

Limits to magnetic resonance microscopy

Paul Glover and Sir Peter Mansfield

Magnetic Resonance Centre, University of Nottingham, Nottingham, NG7 2RD, UK

E-mail: Paul.Glover@Nottingham.ac.uk

Received 16 May 2002, in final form 31 July 2002

Published 30 August 2002

Online at stacks.iop.org/RoPP/65/1489

Abstract

The last quarter of the twentieth century saw the development of magnetic resonance imaging (MRI) grow from a laboratory demonstration to a multi-billion dollar worldwide industry. There is a clinical body scanner in almost every hospital of the developed nations. The field of magnetic resonance microscopy (MRM), after mostly being abandoned by researchers in the first decade of MRI, has become an established branch of the science. This paper reviews the development of MRM over the last decade with an emphasis on the current state of the art. The fundamental principles of imaging and signal detection are examined to determine the physical principles which limit the available resolution. The limits are discussed with reference to liquid, solid and gas phase microscopy. In each area, the novel approaches employed by researchers to push back the limits of resolution are discussed. Although the limits to resolution are well known, the developments and applications of MRM have not reached their limit.

1. Introduction

The field of magnetic resonance imaging (MRI) appeared in 1973 when Mansfield and Grannell [1] described the process, and Lauterbur [2] published the first two-dimensional image. These first imaging experiments were necessarily in the ‘microscopy’ regime, the respective laboratories being equipped only with narrow access electromagnets designed for spectroscopy. After these initial reports, many groups reported increasingly higher quality images and methods, with the major objective being human whole body imaging. High-quality superconductive magnets coupled with improvements in computing and electronics allowed this goal to be realized, with the result that medical MRI is now commonplace in hospitals worldwide. With the development of mainly clinical MRI occupying the attentions of most groups, the imaging of smaller biological or other samples became the preserve of only a few. Interest in the field was re-awakened by the publication in *Nature* of an image of a toad’s egg [3]. This ‘single cell’ image demonstrated that high-resolution microscopy was possible and of interest to biological scientists. Clinical MRI had, by now, established itself, providing functional (flow, diffusion and perfusion) as well as just morphological information. The scientific community could now see that magnetic resonance microscopy (MRM) could provide dynamic information about the state of the sample which was not achievable with destructive imaging techniques. MRM expanded rapidly in fields such as plant biology, polymers and porous media, aided by the availability of wider bore high-field magnets suitable for imaging. A quest for the highest possible resolution ensued, demanding the highest available magnetic and gradient field strengths. This review will describe the factors which limit the resolution of MRM and will give examples of current application. The paper will outline a few of the emerging techniques which are being pursued at the limits of resolution. It is not the authors’ intention to cover detailed aspects of nuclear magnetic resonance (NMR) or MRI, as they are adequately covered elsewhere [4]. Fundamental aspects are explored merely to demonstrate the limits of MRM.

1.1. Definition of microscopy

A survey of papers presented at several of the recent International Conferences on Magnetic Resonance Microscopy [5] reveals most ‘microscopy’ imaging applications (as labelled by their authors) as having pixel resolutions of better than $100\text{ }\mu\text{m}$. A few papers cited lower resolutions than this, but usually because the application was for human *in vivo* micro-imaging or for nuclei other than hydrogen. Only a small number of papers cite in-plane resolutions better than $10\text{ }\mu\text{m}$ —although total voxel volume is a better indicator (of the order of nanolitres). It does seem to indicate that users are accepting a resolution for their experiment which will give the information they require within a reasonable time—particularly if dynamic processes are being studied. There appear to be more than just fundamental issues to consider when choosing a particular resolution.

2. Principles of MRI

2.1. Resolution

We may consider a two-dimensional object which is a source of photons (either emitted or reflected) as shown in figure 1. As an electromagnetic wave, the photons have an electric field spatial phase component (in phasor notation) of the form $e^{-i\mathbf{k}\cdot\mathbf{r}}$, where \mathbf{k} is the wavevector and \mathbf{r} is the position. Scattering processes, such as diffraction, which place a limit on the eventual

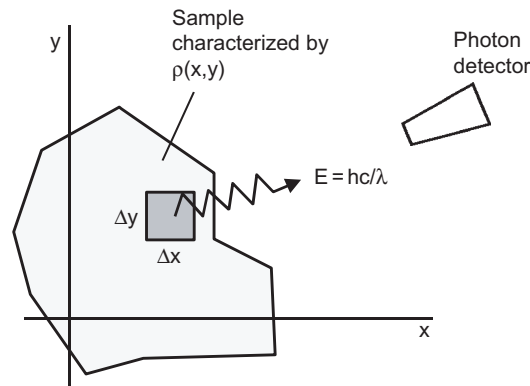


Figure 1. Photon being emitted or reflected from, or transmitted through an elemental area $\Delta x \Delta y$ of a two-dimensional object. The sample is characterized by $\rho(x, y)$, the flux density of photons from the sample as a function of position.

resolution, occur for $k \cdot r \approx 1$. The exact choice of constant is defined by the definition of resolution used, such as the Rayleigh criterion. If an object of size Δx is placed in the path of a plane wave propagating *in vacuo* in the x direction, then there will be an uncertainty in the measurement of its size when $k_x \Delta x \approx 1$. A guide to the limit of resolution is then given by $\Delta x \approx \hbar c / E$, where $E = hc / \lambda$ is the photon's energy, h the Planck constant, λ its wavelength and c the speed of light. For visible light of a few hundred nanometres wavelength, the photon energy is of the order of a few electron volts and resolutions better than a micron can be expected. Electron microscopy is capable of resolutions 100–1000 times better using energies of the order of 10 keV. NMR spin energies are of the order of micro-eV putting the spectral lines firmly in the radiofrequency (RF) band, with wavelengths of metres. How may we resolve just a few microns when the wavelength of the electromagnetic radiation will not allow us to determine the position of a nucleus responsible for the generation of the photon?

2.2. Detection of the NMR signal

The answer to the question posed above is found in the examination of the mechanism used for excitation and detection of the transitions between the energy states of a nuclear spin. The Zeeman splitting results in a slight population excess in the lower (spin $\frac{1}{2}$ for a proton) state at thermal equilibrium [6]. The energy difference between the levels is

$$\Delta E = \gamma \hbar B_0,$$

where γ is the gyromagnetic ratio of the nucleus, \hbar the Planck constant and B_0 the applied constant magnetic flux density. The energy level population difference results in the sample having an overall magnetization (high-temperature approximation) of

$$M_0 = \frac{N_s \gamma^2 \hbar^2 I(I+1) B_0}{3 k_B T_s},$$

where I is the spin quantum number, k_B the Boltzmann constant, T_s the sample temperature and N_s the number of spins per unit volume. For water the available magnetization M_0 is small and represents the maximum signal which can be detected following an excitation pulse. The transitions are induced by a RF magnetic field at the Larmor frequency ω_0 given by $\omega_0 = \gamma B_0$. During the period following this excitation, and while the spins maintain coherence, there is a detectable oscillating magnetic field, due to the excited spins. The resulting free induction

decay (FID) may be detected by a suitable antenna sensitive to the net oscillating dipole moment of the nuclei. Both functions may be performed by a simple solenoid coil enclosing the sample with its axis perpendicular to the orientation of B_0 . RF excitation pulses may be supplied through this coil, and the FID from the oscillating dipoles of the sample nuclei induces an oscillating emf in the coil which is then amplified and recorded. At all practical frequencies the electromagnetic radiation emitted from the sample is vanishingly small and usually neglected. The detector can be said to be working in the inductive or near field limit. The coil forms a tuned circuit, together with a capacitor, at the Larmor frequency. A matching circuit allows a fraction of the total available power to be transferred to an amplifier circuit and then on to the spectrometer [4, 7, 8].

The signal received will be proportional to the ability of the coil to couple to the oscillating magnetization vector (being dependent on coil geometry, filling factor and Faraday's law). It makes sense to employ the highest field possible as the magnetization and induced voltage each scale linearly with ω_0 , implying that the signal recorded will scale with the square of the field strength. The sensitivity can be related to a constant of proportionality dependent on the magnetic flux generated per unit current B_1/i . The experimental signal to noise will depend on the type of imaging sequence employed, but the fundamental source of noise can be attributed to the thermal noise of the sample and detector coil. The root mean square (RMS) noise voltage of a resistance R is given by

$$\sqrt{4k_B T_c \Delta f R},$$

where Δf is the total measurement bandwidth and T_c the effective temperature. While the coil resistance R is shown as a constant, this is not necessarily true as it could have both a frequency dependence ($\omega_0^{-1/2}$ due to skin depth) and a sample dependence. The circulating currents induced in a slightly conductive sample by currents in the coil will dissipate energy and increase the effective resistance of the coil. In microscopic imaging regimes the interdependence of these effects is not clear cut, but below around a 10 mm coil diameter and 400 MHz it is the coil's own resistance which will dominate. As frequencies are also generally high for microscopy, the skin depth of the wire used will serve to increase effective resistance. The coil is also affected by inter-turn capacitances which limit the number of turns and the sensitivity [7]. The quantity which reflects signal-to-noise ratio (SNR) for the coil is therefore $B_1/i\sqrt{R}$. As we shall see, this factor will be compromised by the physical requirements of microscopy.

2.3. MRI resolution

It will be helpful to introduce some of the imaging concepts which will help to define the limits of microscopy. Resolution may be defined in terms of a k space wavenumber $akin$ to an electromagnetic wave, as discussed earlier. To resolve spatially the object proton density a magnetic field gradient is applied. The resonant frequency of a proton at a position \mathbf{r} is now

$$\omega_0 + \omega(\mathbf{r}) = \gamma B_0 + \gamma \mathbf{G} \cdot \mathbf{r},$$

where \mathbf{G} is a magnetic field gradient treated as a vector. The received signal is demodulated to base-band and detected using a quadrature phase sensitive detector, sampled and processed by the demodulator. The sampled signal now contains position sensitive information only, namely $\omega(\mathbf{r}) = \gamma \mathbf{G} \cdot \mathbf{r}$. We may now express the angular frequency as a rate of change of phase and write $\Delta\phi(\mathbf{r}) = \gamma \mathbf{G} \cdot \mathbf{r} \Delta t$ where $\Delta\phi$ is the phase accumulated during the interval Δt . If the wavenumber increment is defined as $\Delta\mathbf{k} = \gamma \mathbf{G} \Delta t$, then $\Delta\phi(\mathbf{r}) = \Delta\mathbf{k} \cdot \mathbf{r}$. The Nyquist sampling theorem defines the limit of resolvable phase as π radians, occurring either at largest \mathbf{r} and minimum increment $\Delta\mathbf{k}$, or vice versa. The first case defines the field of view of the object as $|\mathbf{r}_{\max}| = \pi/|\Delta\mathbf{k}|$ (dependent on sampling interval) and the resolution as $|\Delta\mathbf{r}| = \pi/|\mathbf{k}|_{\max}$

(dependent on number of points times the sampling interval). The expression for the recorded signal for a sample proton density $\rho(\mathbf{r})$, neglecting relaxation terms, is given in terms of the wavenumber \mathbf{k} as

$$\tilde{S}(\mathbf{k}) = K \int_{\text{sample}} \rho(\mathbf{r}) e^{-i\mathbf{k} \cdot \mathbf{r}} d\mathbf{r},$$

where K is a normalization constant embodying sensitivity terms and units. The character of the phase–position relationship gives a clue as to how the resultant signal may be encoded to yield spatial information. The spatial map is obtained from a Fourier transform of the k space data,

$$\rho(\mathbf{r}) = \frac{1}{\sqrt{2\pi}} \int_{k\text{space}} \tilde{S}(\mathbf{k}) e^{i\mathbf{k} \cdot \mathbf{r}} d\mathbf{k}.$$

We therefore need to collect information from the whole of k space to reconstruct the image. To collect data as a function of k , we may allow the signal to evolve while a constant gradient is present, i.e. a gradient in the x direction would acquire data in the k_x direction of k space. A similar effect could be achieved by a set of impulses of the gradient thus ‘moving’ the k space point in a stepwise fashion along the k_x axis. The former is referred to as ‘frequency’ encoding and the latter as ‘phase’ encoding. There are many and varied pulse sequences for obtaining this basic k space map [4, 8]. The number of spatial axes encoded might be one, two or three, all with an independent selectable resolution and field of view. Some imaging schemes make assumptions about the k space data or information content to reduce total imaging time or improve apparent SNR. As we are not bound by the resolution imposed by the frequency of our NMR signal, it would appear that we may choose any resolution we wish, e.g. a (not unreasonable choice of) gradient of 100 mT m^{-1} and an acquisition time of 100 ms would yield a resolution of $1 \mu\text{m}$. Most users of MRM clearly do not achieve this, so what practical issues prevent this limit being reached?

In the example quoted, and in the analysis above, intra-voxel phase coherence of the signal has been assumed. There are several effects which render this assumption untrue. Simple spin–spin (T_2) relaxation processes reduce the transverse magnetization exponentially as a result of random spin flips. Gradients which are independent of the spatially encoding gradients de-phase the spins during the acquisition period and although this process in liquid-like samples is reversible to some extent, this will prove to dominate the achievable resolution. Movement of the sample itself, either by flow processes, self-diffusion or vibration, causes attenuation of the image. Spin-lattice relaxation (although not affecting the decay of the signal) severely restricts the speed at which one can repeat the acquisition so has a role to play in the determination of the image SNR, per pixel available in a unit time. It is undoubtedly the image SNR which determines the choice of resolution. To double the SNR, the number of signal samples would have to be multiplied by 4. Doubling the resolution in two dimensions would divide the pixel SNR by 4, therefore requiring an average of 16 signal samples to restore the original SNR. At some point the resulting image quality becomes unacceptable. By considering the Fourier relationship between k space and frequency, the signal and noise per resolved point may be expressed in terms of k_{max} . For a particular SNR to be maintained (ignoring any relaxation effects), we obtain the relationship $\Delta r \propto G^{1/3}$. This surprising result indicates that *higher* resolutions may be obtained with *lower* gradients. This is contrary to all MRM practice, so further factors must be included.

If we now consider signal decay as a multiplier of our NMR signal, then the resulting image will be convoluted with a point spread function (PSF) derived from the Fourier transform of the attenuation characteristic. For a simple mono-exponential (having a time constant τ), this PSF will be a Lorentzian having a full width at half maximum of $2/\tau \text{ s}^{-1}$. If this relaxation process

dominates, then we may set the maximum allowable $T_{\text{acq}} = \pi\tau/2$. In NMR, the transverse or spin-spin relaxation time constant is designated T_2 and characterizes this signal decay. For soft biological tissues, the values of T_2 may lie in the region of 10–100 ms. However, at the high fields employed for microscopy it is other, sample related, effects which may dominate. Susceptibility differences between tissues, and, in particular, at the interfaces lead to local gradients and hence field inhomogeneity. In microscopy the effective T_2^* may be as little as a few ms giving a resolution of $\Delta r = 2/\gamma G T_2^*$. In this relaxation limited resolution case, for constant SNR we have $\Delta r \propto G^{-1}$. This now competes with the previous requirement for the gradient. Biological specimens are particularly prone to limits imposed by tissue water translational self-diffusion (D). The RMS displacement of a molecule undergoing diffusion in the period T is

$$\sqrt{\langle r^2 \rangle} = \sqrt{6DT}.$$

Whereas this will not affect macroscopic imaging unduly we see that, for $D = 1 \times 10^{-9} \text{ m}^2 \text{ s}^{-1}$ and $T = 10 \text{ ms}$, the RMS molecular displacement is $7.7 \mu\text{m}$. We see that choosing a resolution for our image at or less than $7.7 \mu\text{m}$ will be impossible. In addition, intra-voxel molecules move randomly and independently, each acquiring a random phase. The decay of the resulting signal is not mono-exponential but has the form $\exp(-\alpha\gamma^2 G^2 D t^3)$ where α is a sequence-dependent constant. Again to maintain SNR and without compromising the resolution, the magnitude of the exponent term should not exceed unity. Relating this to the resolution we obtain $\Delta r \propto G^{-1/3}$.

The relationships developed above may be visualized in figure 2 (after Callaghan [4]) which shows $\log(\Delta r)$ plotted against $\log(G)$ for constant SNR. This serves to illustrate the limits imposed by relaxation, diffusion and the systematic limit. The absolute position of the slope will scale with the parameter indicated. The optimum resolution for any given parameters can be determined. For example, the highest resolution biological imaging will probably be dominated by self-diffusion, whereas the imaging of soft solids may be limited

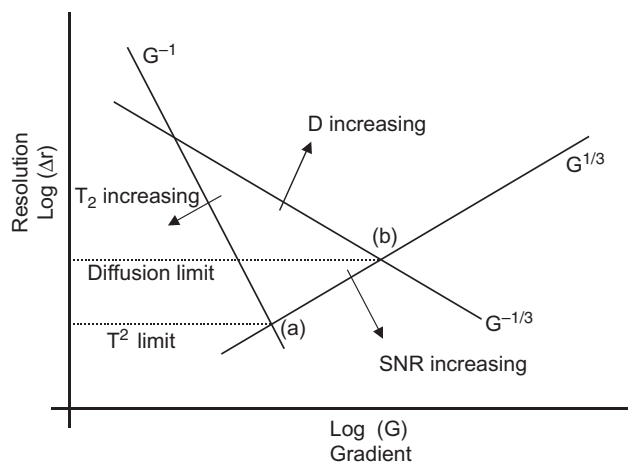


Figure 2. Relationship between resolution and gradient for constant image SNR for a range of regimes. The parameters which govern each boundary are shown together with the direction that an increase in value would move that boundary. The intercepts of the boundaries define (a) the T_2 limit and (b) the diffusion limit. The possible areas of operation lie above these lines. These boundaries are not as sharp as depicted, and they may be crossed, but with a severe penalty in additional imaging time.

by either the natural T_2 , or the T_2^* of the sample and magnet. Self-diffusion (both translational and rotational) and T_2 will both be linked to mobility of the molecules containing the nuclei of interest. In general, these have an opposing effect on our allowable resolution. For example, samples having low self-diffusion coefficients tend also to have short T_2 values. The latter is due to the long molecular motion correlation time.

In the preceding analysis, no account has been taken of the spin-lattice relaxation time T_1 . In general, long values of T_1 will serve to limit the overall image SNR per unit time, as it governs the rate at which scans of k space may take place. In essence, there is an optimum repetition time related to the type of scan being performed and the relaxation time. The magnetic resonance (MR) microscopist may choose to optimize scan time and sequence for the image information required. As the image contrast depends on certain fundamental parameters, these may also be measured both quantitatively and qualitatively. The image resolution may therefore be set by the user to either militate or mitigate limiting effects. In any MRM experiment, the user wishes to maximize the useful information content, and minimize the uncertainty of a measurement, in a given time. For example, the sample may be changing or moving which will require a faster imaging time. Signal-to-noise, parameter measurement and resolution may be traded for speed of image acquisition in most cases.

3. Coil and gradient design for microscopy

The above analysis shows that the available image resolution depends critically on the available SNR and gradient strengths available. In general, for the very highest resolution a combination of high magnetic field strength (> 10 T), high gradient field strength (in region of 1 T m^{-1}) and a highly sensitive RF coil having a high filling factor (90% if coil encloses whole sample, or a surface coil which is optimal for a region of interest) is required. In this section, the technology developments that define the sensitivity and gradient strength, which, in turn, define the eventual resolution, are discussed.

3.1. RF coils

One of the major constraints of the RF coil geometry is usually that imposed by the sample requirements. This aspect is particularly true in biological applications where samples need to be kept viable, either alive or perfused if *in vitro*. The sample also needs to be insulated from the coils and requires some sort of carrier or holder—which may constrain the filling factor. As researchers have attempted to reach single cell resolutions, then the practical difficulty of placing the sample in the correct position for subsequent imaging arises.

For a highly efficient RF coil it is the function $B_1/i\sqrt{R}$ which will reflect the overall SNR [9, 10]. It is obvious that this may be achieved by maximizing B_1/i , minimizing \sqrt{R} , or a combination of both. The former may be easily optimized but will be compromised by the sample, e.g. it is not possible to insert a large sample (small animal) into a transverse solenoid. The use of sub-optimal 'surface coils' has to be used. However, these may be placed only where they are required and some advantage is restored. The graph in figure 3 (after Morris [11]) shows the SNR/volume variation with coil diameter (d). Down to a certain size, the graph has a d^{-1} characteristic as would be expected from a simple calculation. However, below this, the skin depth of the conductor dominates and the gradient is $d^{-1/2}$. Morris estimates that the transition diameter is $d = 300 \mu\text{m}$ at 300 MHz. At diameters less than 2 mm the coil self-resistance dominates, biological samples of normal conductivity having little effect. This latter regime may be exploited further by reducing the self-resistance using high-temperature superconductive (HTS) films to build the coils. A number of researchers have been pursuing

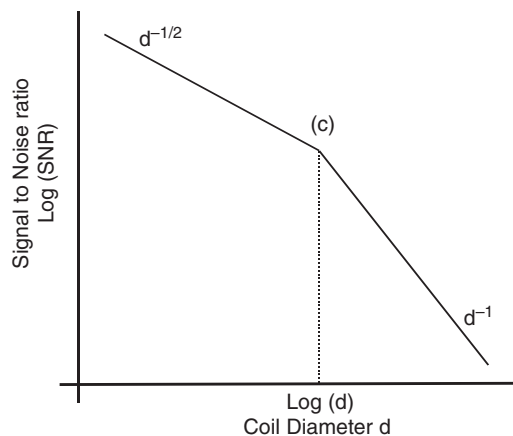


Figure 3. Relationship between SNR per unit volume and solenoid coil diameter in the microscopic regime where sample loading may be neglected. The graph shows how the skin depth effect in the coil wires dominates for small diameters. The intercept at (c) depends on wire type and diameter, geometry and frequency. At 300 MHz this would correspond to a coil of about 300 μm diameter.

this method for microscopy in different regimes. To maintain the superconductor in its low resistance state, the film has to be oriented parallel to the field and at low temperatures. These factors will reduce the filling factor to $\frac{2}{3}$ of that which would be possible using room temperature copper coils but the Q factor ($\omega L/R$) is usually so high that the overall improvement in SNR is quoted at between 3 and 10 times. The disadvantage is the low useable bandwidth for the experiment even at high fields. Ginefri *et al* [12] report a HTS coil based on a loop transmission line which may be used for micro-imaging of human skin *in vivo* on a conventional 1.5 T body scanner. A 40 μm uni-axial resolution perpendicular to the skin is quoted. They report that the expected coil orientation problem is not severe with a misalignment angle of 5° having no perceived effect on the image SNR. Hurlston *et al* [13] report a Helmholtz HTS film coil operating at 9.4 T. In addition, they employ a liquid nitrogen cooled GaAs FET pre-amplifier to bring the total system noise temperature to 90 K. They demonstrate 17 μm plane resolution having an overall image SNR of 29 in an imaging time of 1 h. A similar copper coil at 293 K would have a SNR of around 4. An imaging time of 49 h would be required to match the image quality of the cooled quality. They also report current saturation effects when the coil is used for transmission and that the coil SNR is not as great as would be expected. It is appropriate to point out that only at very low fields would conventional imaging show any benefit from using HTS coils—an avenue being pursued by several researchers and manufacturers. Cooling conventional copper coils down to 77 K also has benefits for micro-imaging *in vivo*, as demonstrated by Wright [14], gaining a useful factor of 2–3 in image SNR.

At very small sample volumes, it becomes increasingly difficult to insulate thermally the sample from the coil and retain the filling factor required to make the HTS approach viable. For the very highest resolutions reported it would appear that the construction of micro-coils is the only alternative. This approach has been taken in the field of spectroscopy, and while not strictly imaging, it is of relevance as the overall total sample volume is on a scale of nanolitres and may have some bearing on imaging at these scales. An example of this approach is a planar loop coil of inner diameter 50 μm which has been etched or micro-machined on to a glass or a GaAs substrate [15]. A 100 nl sample chamber has also been etched into the substrate. High-quality proton spectra have been recorded in a few minutes. The authors point out the possibility of integrating the pre-amplifier onto the same substrate, therefore cutting

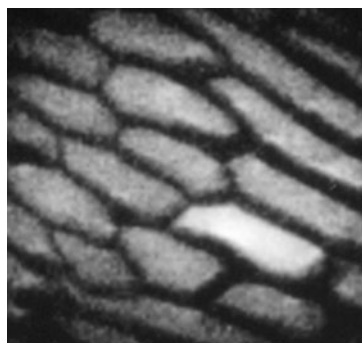


Figure 4. Single cell thick sheet of onion cells obtained using the microscope slide coil at a field strength of 11.7 T. The image resolution is $7.5\ \mu\text{m}$ and took 100 min to acquire. The air spaces were filled with CCl_4 which produces no signal. Individual cells can be identified both optically and from the MR image (first published in [18]).

down the effective resistance of the coil. This would be particularly advantageous if the active device could be matched to the coil impedance and the Q defined by an external circuit. This would overcome one of the difficulties with micro-coils, in that the small inductance has to be tuned using a large (physical size and value) capacitance. There are clear benefits in reducing sample volume sizes for spectroscopy, for example, in the case of difficult-to-extract metabolites. Olson *et al* [16] describe the detection of spectra from a stopped flow electrophoresis tube.

Sometimes, the geometry or the handling of the sample imposes a particular constraint upon the coil, or additional sensory information is required. An example of this approach would be the microscope slide coil [17, 18] where a loop coil has been integrated within a conventional optical glass slide. The probe maintains an optical path through the slide so that the sample may also be imaged using an optical microscope. This approach allows for accurate sample placement and single cell imaging. A single cell thick sheet of onion epidermis was imaged using this coil with an in-plane resolution of $7.5\ \mu\text{m}$, and is shown in figure 4. Wind *et al* have recently taken this concept a stage further, and they describe a simultaneous high-resolution MRI and optical confocal microscopy system [19]. Both the optical and MR images presented have similar resolutions of just a few microns. They demonstrate how data fusion techniques can enhance the information content of each imaging regime—adding value to both MRM and complimentary modalities.

The primary requirement for RF B_1 generation is that it is oriented perpendicular to the B_0 axis (conventionally z), so may lie anywhere in the x – y plane. It is usual to fix the coil but Roffmann *et al* [20] report a coil which may tilt to any angle (measured from the z axis but with B_1 always along the x axis) without degradation of performance. The ‘tilt’ may be used to simplify small animal handling capabilities. This coil (working at 750 MHz and 17.6 T) may also be used to investigate tissue anisotropy. Because dipole–dipole interactions have an angular dependence, an additional image contrast mechanism is introduced. For example, the T_2 maps obtained from cartilage show this behaviour indicating an alignment of tissue structures [21].

3.2. Magnetic field gradient coils

The issues affecting gradient design for microscopy are similar to those encountered at larger scales. These issues are coil efficiency, gradient homogeneity, gradient strength, active

screening and vibration. The current required for a particular gradient strength will scale as the inverse cube of the coil diameter. However, the wire resistance will increase as it becomes increasingly harder to fit the wires on to the coil former (proportional to the cube of the efficiency). The ensuing power losses seen as heating will either limit the duty cycle of the gradient or the time before failure of the unit. Bowtell and Robyr [22] propose a layered winding approach which relaxes the cubic law slightly, thus allowing a transverse gradient to be constructed which will produce gradients of up to 10 T m^{-1} over a 6.5 mm radius whilst having an instantaneous dissipation of 650 W. Seeber *et al* [23] describe a full three-axis gradient set capable of producing over 12 T m^{-1} with a dissipation of around 330 W. This gradient will be able to achieve $1\text{--}2 \mu\text{m}$ resolution in biological samples (i.e. upper limit set by diffusion) provided that the SNR is adequate. The transverse gradient coils are single pairs of conductors set at right angles in the $x\text{--}y$ plane—as shown in figure 5. The inductance is very low, allowing fast gradient switching speeds. However, the power dissipated by passing the large current required will only allow gradient pulses of a few milliseconds at a reasonable duty cycle. The gradient homogeneous volume is smaller than the coil described earlier but this is not seen as a disadvantage because of the intention to image over a very small field of view. This author also describes a method of winding a coil on a micro-pipette having an outer diameter of less than $100 \mu\text{m}$, the coil having 5 turns of $20 \mu\text{m}$ diameter wire.

Taking this approach a step further, Zhang and Cory [24] have designed switched gradient coils (1, 4 and 31 turns) capable of generating fast-switching gradients up to 600 T m^{-1} . These gradients are not intended for imaging, but for solid-state spin-diffusion measurements. A gradient field generates a spatial modulation of the magnetization across the sample. This pattern may be utilized in a manner similar to a diffraction grating having a period of between 1 nm and $1 \mu\text{m}$.

Several authors have proposed using RF field gradients to impose spatial and diffusion modulation on the sample [25]. This novel approach has the particular advantage in

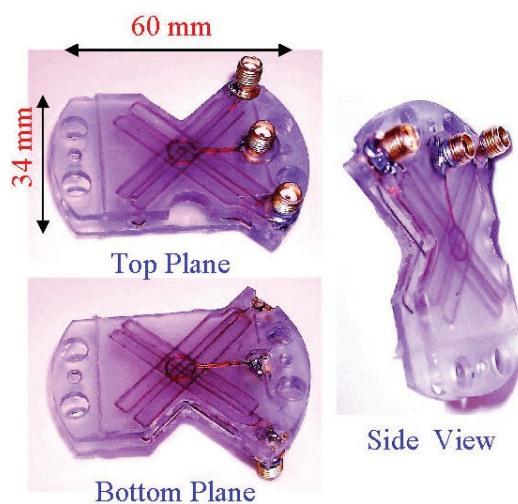


Figure 5. Photograph of the single-turn tri-axis micro-coil gradient system designed by D Seeber. A previous version of this coil is described in [23]. The wires are now placed in a polycarbonate coil form and then sealed with liquid acrylic. The straight wire x and y gradients, as well as the Maxwell pair z gradient windings can be clearly seen. The RF micro-coil is not shown, but this slots into position between the two acrylic plates supporting the gradients. (Photograph courtesy D Seeber, Ohio State University, USA.)

microscopy in that the images or diffusion maps are less susceptible to background gradient inhomogeneities arising from susceptibility interfaces. Using conventional gradients only an apparent diffusion coefficient (ADC) may be measured whereas Valtier *et al* [26] show that, by using a B_1 gradient of 50 T m^{-1} , a true diffusion map may be obtained. A resonant RF field gradient has the advantage of having a Q multiplication of the net flux obtained over that obtained with directly driven coils—hence the apparently high gradient. This approach lends itself to a wide range of diffusion measurement problems in porous media and other samples with interfaces.

4. Current state-of-the-art

In the above review of technology, the examples chosen represent the highest resolutions or sensitivities currently available. In this section, the phases of condensed matter are examined separately as each has different limiting factors, and hence different applications and approaches.

4.1. At the limit of liquid state

It is reasonably safe to say that, in the liquid state, it is self-diffusion which limits the realistic image resolution. In addition, one particular problem that affects mainly MRM is that of sample-dependent field gradients caused by susceptibility differences between materials. These differences (of the order of 1 part in 10^8) are enough to cause gradients of 10 T m^{-1} or more near to interfaces. At best, parts of the image will simply be shifted and appear in the wrong place. At worst, the signal will be lost altogether because of diffusion in such a strong gradient [4, 17]. In plants, air spaces between the cells lead to particularly high susceptibility differences. This explains the ‘blotchy’ nature of the plant images, the air–cell interface appearing much larger than it really is, as seen in figure 4.

Plant biologists are now using MRM to gain information about the function of plants, e.g. how metabolites are transported, stored and processed [27]. For example, chemical shift imaging of the proton peak associated with sucrose results in a map showing storage and transport within the phloem. Additional techniques, such as cyclic cross-polarization may be employed to map a particular sugar or metabolite of low abundance [28]. These examples are reproduced in figure 6. In a paper by Olt *et al* [29], direct imaging of sodium in certain plant systems can be used to demonstrate, for example, how salt damages plant tissues. Plants may be developed which are salt tolerant. These plants will have many benefits for populations in arid areas. MRM can quickly measure salt kinetics in intact tissue—which is not possible using auto-radiography and freeze sectioning. Uptake in various tissues may be monitored over the course of a day with good temporal resolution. A spatial resolution of $156 \mu\text{m}$ is chosen which gives acceptable images in around an hour. Sodium has a relative sensitivity of about 10% compared to that of protons.

In general, plants (apart from seedlings or seeds) do not lend themselves to MRM. It would be far more useful to be able to take the imaging system into the field. The true power of MRI and spectroscopy is its ability to make measurements on intact systems. Indeed, many researchers who class themselves as ‘microscopists’ do not quest the highest resolution or highest static or gradient magnetic fields. However, all NMR exponents the world over work at the limit of the SNR available at their chosen magnetic field. For example, Haishi *et al* propose a small portable imaging system capable of $50 \mu\text{m}$ in-plane resolution images of high quality in a few minutes, and $200 \mu\text{m}$ isotropic three-dimensional images in 1 h. This would be unremarkable at high field but such images were obtained using a 1 T permanent magnet

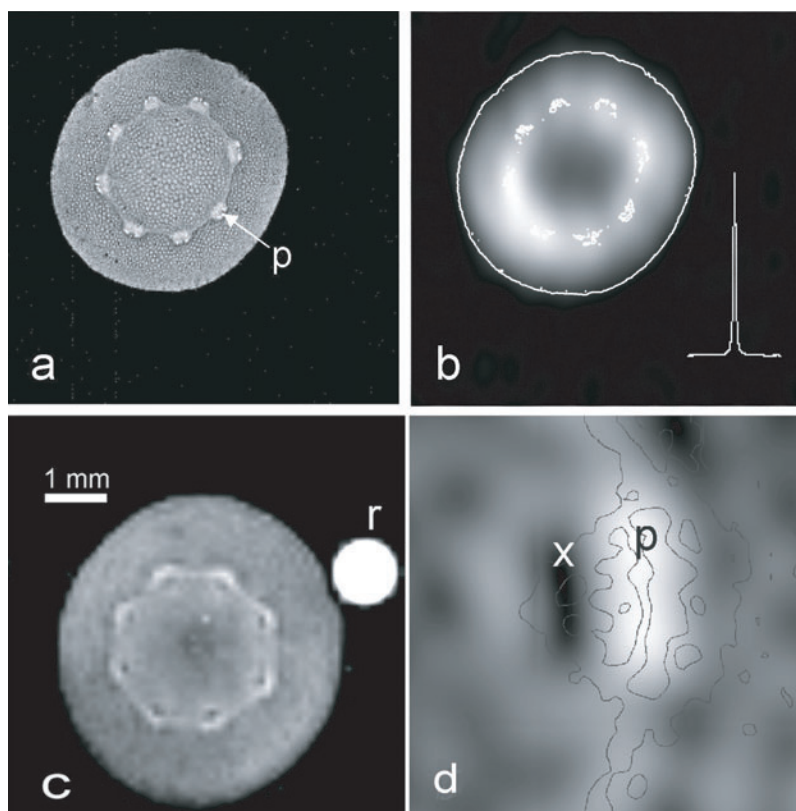


Figure 6. (a) High-resolution proton image from the hypocotyl of a 6 day old castor bean (*Ricinus communis*). The 'p' identifies the phloem within one vascular bundle. The scale bar is 1 mm. (b) The indirectly detected ^{13}C from the C1' position of sucrose is mapped using a cross-polarization technique. This uses the higher abundance of protons to enhance the signal above that obtained using direct detection. The in-plane spatial resolution of this map is $500\ \mu\text{m}$. The phloem bundles have been highlighted. (c) A proton chemically selective image map from the spectral line associated with the C6 of the glucose and fructose moieties within the sucrose molecule. The in-plane resolution is $94\ \mu\text{m}$ corresponding to a volume of 17.5 nl, taking 3.5 h to obtain. The reference 'r' is 200 mM sucrose solution. (d) A detail of the vascular bundle showing high sucrose concentrations in the phloem, and very little present within the xylem. (Images reproduced courtesy of W Köckenberger, Nottingham.)

and low-cost spectrometer [30]. The relative portability of such a system would allow on-site or *in situ* measurements for quality control purposes of, for example, foodstuffs.

At the opposite extreme in terms of acquisition time, sequences based on echo planar imaging (EPI) can be used for imaging at both high speed and high resolution. Peters and Bowtell [31] demonstrate single-shot images of phantoms and biological samples using EPI at 11.7 T. These images take less than 100 ms to acquire, and have an in-plane resolution of better than $100\ \mu\text{m}$. They argue that this unparalleled temporal resolution makes possible real-time microscopy of dynamic processes such as mixing and flow. The resolution available using this technique is effectively limited to around $30\ \mu\text{m}$ —again because of self-diffusion.

Currently, the highest in-plane resolution liquid state published images may be found in a paper by Lee [32]. This paper reports $1\ \mu\text{m}$ in-plane resolution; however, the liquid used for the phantom is an oil with a low self-diffusion. The image obtained and demonstration of

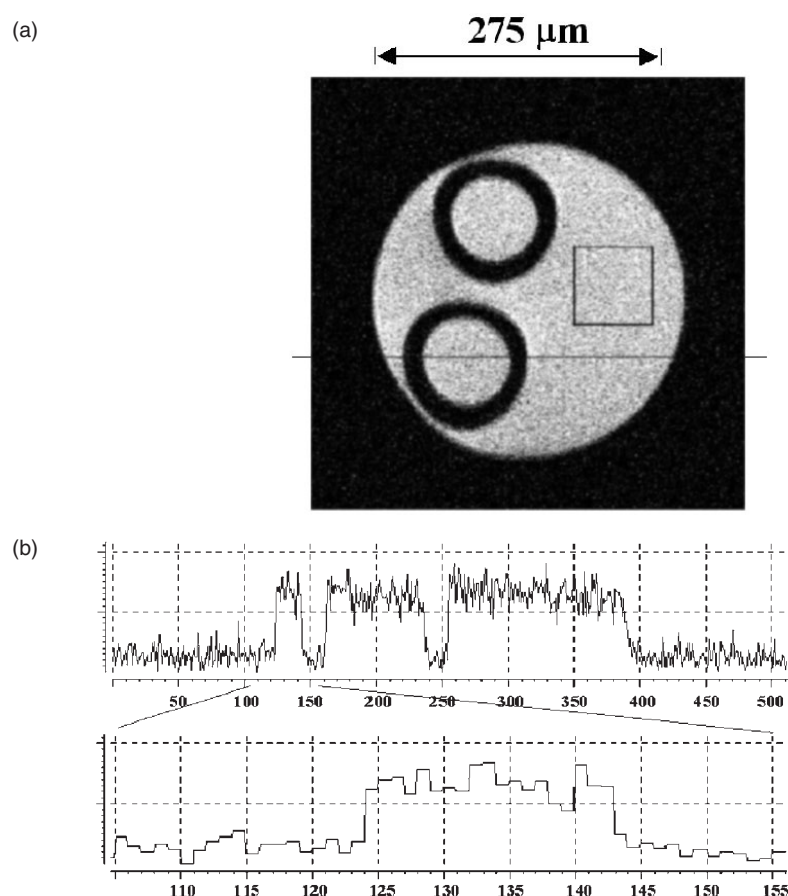


Figure 7. (a) Tube containing mineral oil and two capillary tubes. The image has a voxel size of $1 \times 1 \times 75 \mu\text{m}$. The total imaging time is 56 min. (b) Line profile of pixel intensity along the horizontal line is shown in (a). An expanded portion at an edge of the tube is shown to demonstrate the true in-plane resolution obtained. (Images reproduced courtesy of S Lee, KAIST, Korea.)

this resolution is reproduced in figure 7. Also in this paper, the authors present high-quality images of geranium stems at $2 \mu\text{m}$ resolution.

Clearly, if quantitative measurements of self-diffusion D are required, then a somewhat lower image resolution has to be accepted. The image intensity will be attenuated by a weighting factor of $\exp(-bD)$ where b is a sequence-dependant value proportional to the square of the gradient. To determine D to a reasonable degree of accuracy, several images are obtained using a range of b values. Intensity values, on a pixel-by-pixel basis are fitted to either a mono- or bi-exponential fit to yield values for D . Grant *et al* [33] demonstrate in *Aplysia Californica*, image guided measurements of ADC within a neuron *in vitro*. The diffusion weighted images have a basic in-plane resolution of $40 \mu\text{m}$ and small regions of interest (comprising 5 pixel, equivalent to about 1 nl) may be selected to determine the ADC separately of both the nucleus and cytoplasm within the cell. The ADC of the nucleus has a higher value than that of the cytoplasm, and both are significantly lower than the saline surrounding the cell.

As imaging techniques have been refined over the past decade, there has been an increasing interest from biologists to harness that power to determine tissue function or performance. It

would not be possible, in such a general review as this, to cover all aspects of the work going on worldwide. There is work being carried out in brain function and biochemistry, transgenics and developmental biology to name a few areas. In the remaining part of this section, four particular examples have been chosen.

MRI exploits the changes in NMR spin relaxation times brought about by slight changes in molecular environment. For soft living tissues, the resulting effects on the NMR signal give an image contrast even though the proton density is quite even. As an example, figure 8 shows the development of a *manduca* moth, whose caterpillar stage is called the *tobacco hornworm*. The single section is part of a three-dimensional data set collected during the 16 day development cycle. The chosen section shows the development from the simple eye of the caterpillar, to the compound eye of the insect. It should be pointed out that the set of images shown in figure 8 are a registered fusion of images from a number of specimens—but in principle, a single insect development could be followed. Whilst higher resolutions could be obtained using optical techniques, such an approach would require many moths to be sacrificed. In the case of caterpillars, this may not be a problem, but for rare species, higher species or transgenics research, this would be unacceptable. Images can be produced for any arbitrary plane, clearly impossible to achieve with any great accuracy using a destructive technique. There is also the opportunity to obtain spectroscopic or other information during the development.

Currently, the highest magnetic field being used for microscopy is 17.6 T corresponding to 750 MHz for protons. At such high fields, not only is the available SNR higher, but contrast due to relaxation is also enhanced. Hogers *et al* [34] show that, in a study of chicken embryos, high-resolution images of the embryo vasculature can be obtained. They carried out identical imaging protocols on both 7 and 17.6 T spectrometers, showing that the image contrast-to-noise ratio increased by a factor of 3.5 at the higher field. A three-dimensional image data set having 55 μm isotropic resolution and 14 mm field of view was obtained in 14.5 h. The images shown in the paper are maximum intensity projections and clearly show the development of the major arteries and veins (figure 9). They expect further improvements in techniques at this higher field strength, which will enable researchers to study embryos *in vivo* and hence to examine cardiovascular anomalies during embryo development. Hogers points out that, because MR is non-deleterious, valuable samples can be analysed subsequently using other complementary techniques.

The sensitivity of the MRI experiment to the movement of fluids can be used to quantify diffusion (as already described), flow and perfusion. Bauer *et al* [35] describe a rapid perfusion measurement technique based on the relationship between T_1 and tissue perfusion. This relationship arises because of the differences between the stationary and the in-flowing blood in the selected slice being imaged. A perfused, isolated and beating (>300 bpm) rat heart was imaged using a rapid T_1 prepared technique. Sixteen images of 140 μm resolution were obtained using different inversion recovery weightings to yield the T_1 maps in less than 40 s. The tissue perfusion within the myocardium can then be calculated from the T_1 maps. These measurements were performed without a gadolinium-based contrast agent—the usual method for perfusion measurements. The work aims to throw light on the poorly understood fractal nature of heterogeneity of myocardial blood flow, and hence the microvascular tone.

It is usual for x-ray computed tomography (CT) to be the method of choice for looking at, for example, bone structure and bone density. However, MRI and microscopy may also be used to study the trabecular structure of bone at better resolutions than those generally available using micro-imaging CT systems. In the case of MRM, it is the fluid-filled pores which produce the image—the bone structure then being deduced from the ‘negative’. This indirect method yields three-dimensional images (around 40 μm resolution) of bone structure in around 10 h for excised mouse tibia (Gardner *et al* [36]). The purpose of Gardner’s experiment is to measure

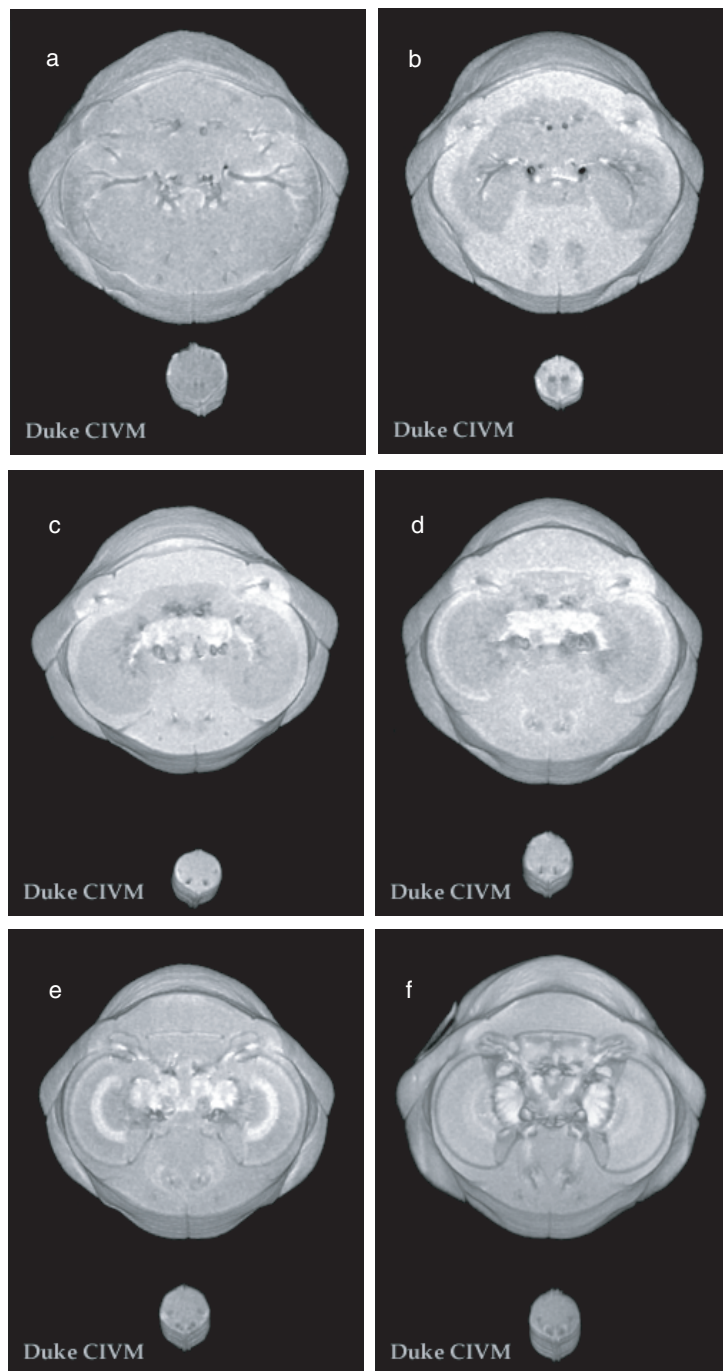


Figure 8. Series of images showing the metamorphosis of a *tobacco hornworm* caterpillar into a *manduca* moth. This slice shows the development of the compound eye. The images were taken at (a) 1 day, (b) 4 days, (c) 7 days, (d) 10 days, (e) 13 days and (f) 16 days after pupation. (Images reproduced courtesy of F Nijhout and S Gewalt, Duke Center for *In Vivo* Microscopy, an NIH/NCRR National Resource.)

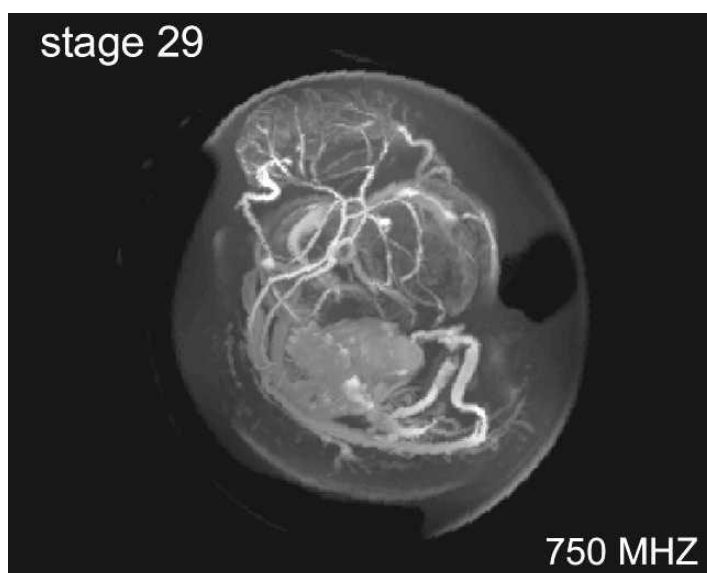


Figure 9. Maximum Intensity Projection image obtained at 17.6 T of a gadolinium contrast enhanced chicken embryo showing the venous detail. The resolution of the basic three-dimensional image is $55\ \mu\text{m}$ isotropic and took 15 h to obtain. The cranial vasculature (top) and heart and dorsal aorta (bottom) may be seen. (Image reproduced courtesy of B Hogers, University of Leiden, Netherlands.)

the changes which may occur within trabecular structure during conditions of microgravity (simulated by suspending the limb). Changes in bone volume and trabecular spacing was found to be similar to those reported by studies of rats flown in space and subsequently analysed using optical techniques. Many research groups are using MRM to identify and understand the process of osteoporosis.

The examples in this section not only demonstrate the limit of resolution, but also limits to the rate, quality or amount of information collected. It is clearly possible to achieve very high spatial resolution. However, for any measurement of quantitative (or even qualitative) information, some compromise must be accepted. In MRI, the resolution may be explicitly chosen to be lower than the maximum possible, with commensurate improvements in SNR or reduction in imaging times. All parameter measurements (almost without exception) lead to a reduction in image SNR with the parameter weighting. Therefore, working at the limit to resolution *before* introducing the weighting will lead to errors in that parameter measurement. Clearly, researchers applying MRM to particular scientific questions wish to maximize the information obtained, either per unit time or per sample, within the constraints set by the sample.

4.2. At the limit of solid state

The solid state presents new problems for imaging compared with the liquid state. Although diffusion coefficients are low, thus relaxing this particular constraint, the T_2 relaxation times are considerably shorter. The short relaxation times arise because of the dipolar coupling between spins within a more rigid lattice which is not motionally averaged compared with a liquid. Consequently the resolution is always limited by the broad lines of the NMR spectra. For crystalline solids, the T_2 may be just a few microseconds, resulting in spectral lines that are

several kilohertz wide. Generally, there are two options available to the investigator wishing to overcome this broadening: either narrow the lines by 'switching off' the coupling terms or impose extreme gradients that dominate the broad line. The review articles by Demco and Blümich [37, 38] describe both the theory and method of these techniques in more detail.

Many line-narrowing techniques have been developed for spectroscopy of solids, but these are sometimes difficult to integrate into imaging sequences. Chingas [39] and Miller [40] describe how multipulse line-narrowing methods such as MREV8 may be combined with a Zeeman or spin-lock element, together with spatial encoding to give images of polymers and elastomers. Line narrowing using magic angle spinning (MAS) may be combined with imaging to achieve a reasonable resolution [41]. In this case, the sample is spun at several kilohertz at an angle of 54.7° away from the axis of the main field. The imaging gradients which are phase locked to the sample spin frequency can now be imposed, thus providing spatial encoding without any dipolar broadening.

Two techniques which fall into the gradient dominated category for high-resolution imaging of near solid samples will be mentioned here. One of these is the stray field imaging (STRAFI) method [42, 43] which makes use of the very intense axial gradient present just a few centimetres away from the iso-centre (i.e. the homogeneous field region at the centre of the magnet where most imaging or spectroscopy takes place). For example, a 9.4 T, 89 mm bore magnet will have a gradient of 58 T m^{-1} superimposed on a field of 5 T at this point. This large fixed gradient allows the user to select a slice of just a few microns thick without line broadening smearing it out. The sample may be imaged one slice at a time by physically moving the sample or changing the frequency of the spectrometer. Usually the information is collected for one spatial dimension only, because to encode a three-dimensional image would require two rotational degrees of freedom as well as the axial movement. A three-dimensional imaging can be achieved but the power of this technique is in measurement of dynamic processes such as solvent ingress in polymers and other porous media. The samples are usually quite readily turned into a one-dimensional model system. A variant of this technique led to the development of a small permanent magnet (GARField) with curved pole pieces which generate a uniform gradient of up to 20 T m^{-1} [44]. The geometry of this magnet is especially suited to imaging (more correctly, one-dimensional profiling through) thin (up to $400 \mu\text{m}$ thick) film samples such as paint and coatings. The actual spatial resolution of this technique is determined almost entirely by uniformity of the sample and its alignment normal to the magnetic field gradient axis. As an example of MRI of materials, figure 10 shows how a light activated dry latex paint film cures over a period of several hours. Within the film there are two competing processes: light activated crosslinking and oxygen inhibition. As oxygen may only diffuse from the open-to-air side of the film, the cure process starts at the substrate—a process undetected by other tests [45]. The high gradient of the GARField magnet allows self-diffusion coefficients to be measured within a cellulose film only $70 \mu\text{m}$ thick at a profile resolution of $3 \mu\text{m}$ [46].

The other near-solids imaging technique now being exploited is the single point imaging (SPI) method. The idea of constant T_2 weighted imaging is not new, having been introduced by Emid and Creyghton in 1985 [47]. However, it is now being exploited in semi-solid material applications where short T_2 or T_2^* values are coupled with moderate to short T_1 values, whereas true solids have very long T_1 values. This condition certainly holds for 'solids' such as foodstuffs, porous media, polymers and biological materials such as cartilage. In SPI each point in k space is sampled using a single low angle excitation and single point acquisition, the gradient being stepped after each acquisition, each point having the same T_2 weighting. In the SPRITE variant [48], the magnetization is driven into a quasi-steady-state equilibrium, which enhances the contrast due to T_1 in the image (i.e. long T_1 components are attenuated heavily). As the delay between excitation and sample point may be as short as $50 \mu\text{s}$, most

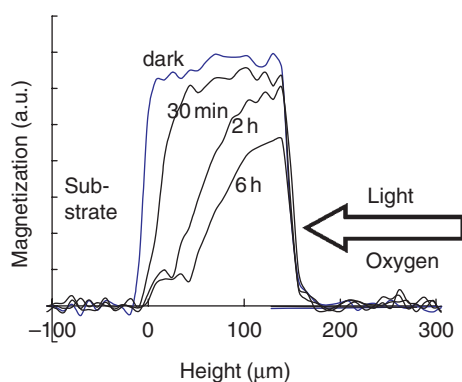


Figure 10. Single dimension depth profiles, taken at various times, on the GARField magnet, of a dry latex film with a photo-sensitive cross-link enhancer added. A light intensity of 1 mW cm^{-2} is used to initiate cross-linking. Oxygen diffusion through the film from the surface works to inhibit cross-linking, and the film 'cures' from the substrate upwards. Each profile through the film has a resolution of $9 \mu\text{m}$ per point and takes 17 min to acquire.

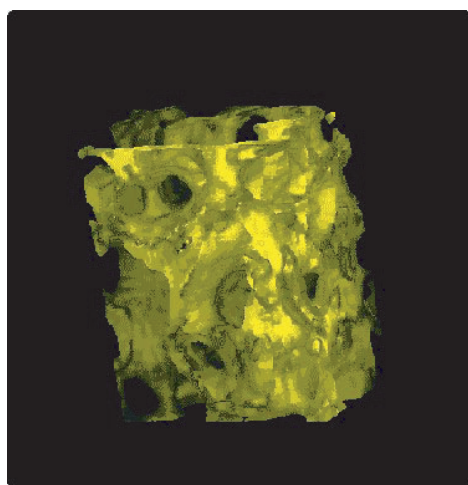


Figure 11. Three-dimensional surface rendered image of oxtail bone structure taken using the SPI technique. The image resolution is $78 \mu\text{m}$ isotropic. The measurement time is approximately 30 h using a 7 T spectrometer. (Images reproduced courtesy of D Höpfel, F H Karlsruhe, Germany.)

polymer systems and porous media may be imaged with high resolution. Variants of this technique allow the user to re-introduce T_1 and T_2 weighting for producing quantitative maps [49]. In the previous section on liquid state imaging, the trabecular bone structure was deduced from images of the pore contents. Figure 11 shows a three-dimensional rendered image of directly detected bovine bone structure using the SPI method [50]. This image has an isotropic resolution of $78 \mu\text{m}$ but took 30 h to acquire at a field strength of 7 T.

A method which falls into the category of solid-state detection using gradient dominated localization is that of magnetic resonance force microscopy (MRFM). Recent developments in ferro-magnetic resonance force microscopy have produced scans of a $3 \mu\text{m}$ thick YIG film [51]. In this technique a small mechanically resonant cantilever is loaded with a small magnetic particle producing an intense local gradient in a nearby sample. When the resonance condition

is met, then a force is exerted on the cantilever. The displacement of the cantilever is measured using a laser interferometer. The RF field is modulated at the cantilever resonant frequency which aids detection due to the mechanical Q of the cantilever. Scanning the tip over the sample, in a manner similar to atomic force microscopy (AFM) then yields a high-resolution spatially resolved map of the sample characteristics. The high-field gradient near the tip gives some control over the depth of the measurement slice within the sample. Barbic [52] describes a variant of MRFM which uses a ferromagnetic sphere oriented such that the dipole moment is parallel to the surface of a crystal. Using this method, an apparent diffraction pattern related to the atomic lattice spacing within the crystal can be observed—interestingly, the original goal of the work of [1].

4.3. At the limit of gas state

Imaging of the gas phase brings together all three major problems facing MR microscopists: low sensitivity (fewer molecules per unit volume than liquids) fast diffusion (4 orders of magnitude greater than liquids) and short relaxation times. These properties can be exploited to probe porous media at different length scales than those explored in the liquid state. For example, gas transport in coal and oil bearing rocks has been studied [53]. Gases such as methane and low molecular weight fluorocarbons may be employed. High pressures can be employed to increase the signal or modify the relaxation times. A gas molecule is much more likely to collide with the surface of a pore, making the NMR characteristics of the ‘probe’ gas change. Modelling of these interactions will yield information about the pore size. Pines [54] describes several uses for gas state imaging in porous media from the nano-scale to the macro-scale and proposes ‘Zero-Field MRI’ using SQUID detectors.

One of the most difficult organs of the body to study using MRI is the lung. Its very function requires its structure to contain air–fluid interfaces. The susceptibility differences (even at low fields) preclude imaging with any real definition. Some studies have reported imaging of the airways with SF₆ at normal pressures and a safe concentration [55] with some success. However, one of the most rapidly growing areas of MR is the applications of hyper-polarized gas imaging. It has long been known that some gases such as ³He and ¹²⁹Xe can be hyper-polarized using spin-transfer of magnetization from rubidium. This can be achieved by tuning a LASER to a wavelength of 795 nm in order to promote transitions of the rubidium nuclear spin to a meta-stable state. The magnetization is then transferred to the gas atoms by collision. The gas is then separated from the rubidium. The resultant magnetization of the gas is many orders of magnitude greater than that of liquids—potentially yielding an image SNR similar to that of liquid state imaging. The T_1 of such a gas is long and the gas may be introduced in small quantities into the airway [56]. Because the magnetization will be destroyed on readout, the imaging techniques used are based on the fast low tip-angle methods. Johnson *et al* [57] has obtained registered three-dimensional helium-3 and proton images of rat lung, with both having in-plane resolutions of better than 100 μ m. The airways on the ³He image may be distinguished down to the 7th branch. Ray traced images of rat lung are reproduced in figure 12. The true resolution of gas imaging is diffusion limited and the authors state that further work is required to characterize accurately the lung tissue. In the case of the lung, as the diffusion becomes more restricted in the smaller airways, surface interaction effects will dominate. However, this can serve to enhance the differentiation of the airway and parenchyma. Already, initial estimates of the effective diffusion resolution limit have had to be revised upwards by an order of magnitude (i.e. from an expected 2 mm to better than 0.2 mm).

Unfortunately, we are unable to hyper-polarize liquids in the same way as gases. However, xenon is soluble in a lipid emulsion, and may then be administered intravenously. Using

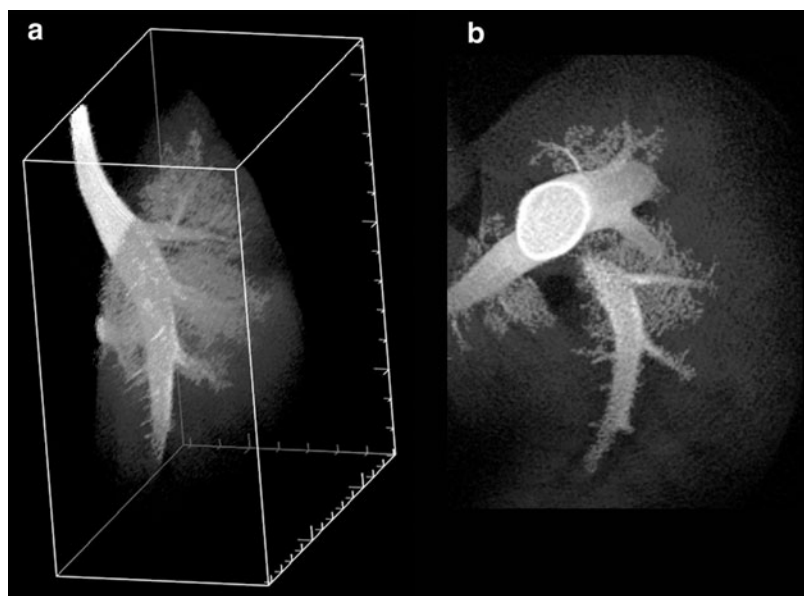


Figure 12. Hyper-polarized helium-3 images of rat lung *in vivo*. A multi-slice image data set is obtained, having an in-plane resolution of $98\ \mu\text{m}$ and slice thickness of $468\ \mu\text{m}$, in just 21 min. (a) A ray-traced display of the right lobe from the multi-slice ^3He data shows the main stem bronchus and branching airways. (b) A magnified rotated view shows smaller airways and microstructure. In this image, note that the edges of the main stem bronchus are enhanced due to diffusion effects. (Images reproduced courtesy of G Allan Johnson, Duke Center for *In Vivo* Microscopy, an NIH/NCRR National Resource.)

radioactive ^{133}Xe as a tracer (in this case administered by inhalation), researchers were able to measure cerebral blood volume [58]. Duhamel *et al* [59] have used HP ^{129}Xe in an emulsion to measure the influx and washout kinetics of the xenon in rat brain, the whole process taking around 1 min. Chemical shift resolved images (at $900\ \mu\text{m}$ in-plane resolution) were obtained, separating the kinetics and location of the dissolved intra-lipid and brain tissue fractions of the xenon.

5. Discussion and conclusions

Despite its early promise, MRM has not shown the same degree of evolutionary advance that has characterized medical MRI. Part of the problem lies in the name which we now acknowledge is a misnomer. The word microscopy engenders the expectation of at least optical resolution. Reality dictates that such a comparison is misconceived. MRM is really about miniature imaging and as such perhaps should be renamed ‘magnetic resonance mini-scopy’.

As we have seen there are no hard and fast limits to MRM. The boundaries are flexible. Nevertheless, there are practical limits imposed by magnetic field strength and imaging time which currently limit practical resolution to about $1.0\ \mu\text{m}$. Ostensibly this limit has been reached. But MRM is about more than resolution.

We have seen that there are many biological applications where resolution ranges from 4.0 to $100\ \mu\text{m}$. These applications exploit the fact that in addition to morphology, MRM can measure a range of other parameters like diffusion, the relaxation parameters T_1 and T_2 , and chemical shift, etc. It is these other parameters which make MRM so useful and important despite its intrinsically poor spatial resolution. We should, therefore, not regard MRM

as competing with optical microscopy but rather as complementing it with additional new information.

There is a wealth of applications for MRM which require detailed, painstaking evaluation. These include micro-spectroscopy, histology and pathology. In biology, plant and animal morphology and physiology have already begun. Evaluation and use of paramagnetic contrast agents together with organ perfusion studies could bring important new insights and applications for MRI in humans.

In porous media, MRM is proving to be an important tool in the study and evaluation of fluid flow in rocks and the oil recovery process in the oil industry. Yet more applications are extant in the food processing industry ranging from mixing of ingredients, slurries, perfusion and diffusion of liquids in cooked products to quality control. It goes without saying that in the pharmaceutical industry, in addition to spectroscopic applications, many of the above mentioned problems occur there as well.

In conclusion, therefore, we may say that in MRM, resolution limits have been reached but the applications of MRM are limitless.

References

- [1] Mansfield P and Grannell P K 1973 NMR 'diffraction' in solids? *J. Phys. C* **6** L422
- [2] Lauterbur P C 1973 Image formation by induced local interactions: examples employing nuclear magnetic resonance *Nature* **242** 190
- [3] Aguayo J B, Blackband S J, Schoeniger J, Mattingly M A and Hinterman M 1986 Nuclear magnetic resonance imaging of a single cell *Nature* **322** 190–1
- [4] Callaghan P T 1993 *Principles of Nuclear Magnetic Resonance Microscopy* (Oxford: Oxford University Press)
- [5] Blümli P, Blümich B, Botto R E and Fukushima E (ed) 1998 *Spatially Resolved Magnetic Resonance* (Weinheim: Wiley-VCH)
- [6] Slichter C P 1990 *Principles of Magnetic Resonance* 3rd edn (Berlin: Springer)
- [7] Chen C N and Hoult D I 1989 *Biomedical Magnetic Resonance Technology* (Bristol: Adam-Hilger)
- [8] Mansfield P and Morris P G 1982 *NMR Imaging in Biomedicine* (New York: Academic)
- [9] Minard K R and Wind R A 2001 Solenoidal microcoil design: I. Optimizing RF homogeneity and coil dimensions *Concepts Magn. Reson.* **13** 128–42
- [10] Minard K R and Wind R A 2001 Solenoidal microcoil design: II. Optimizing winding parameters for maximum signal-to-noise performance *Concepts Magn. Reson.* **13** 190–210
- [11] Morris D, Gorkov P G, Harris A B, Tsao J, Moser K, Georgiadis J, Webb A and Lauterbur P C 1999 Micro-samples, micro-coils, micro-magnets: where will all this smallness end? *L16, In Book of Abstracts for 5th International Conf. on Magnetic Resonance Spectroscopy (Heidelberg)*
- [12] Ginefri J C, Darrasse L and Crozat P 2001 High-temperature superconducting surface coil for *in vivo* microimaging of the human skin *Magn. Reson. Medicine* **45** 376–82
- [13] Hurlston S E, Brey W W, Suddarth S A and Johnson G A 1999 A high-temperature superconducting Helmholtz probe for microscopy at 9.4 T *Magn. Reson. Medicine* **41** 1032–8
- [14] Wright A C, Song H K and Wehrli F W 2000 *In vivo* MR micro-imaging with conventional radiofrequency coils cooled to 77 K *Magn. Reson. Medicine* **43** 163–9
- [15] Dechow J, Forchel A, Lanz T and Haase 2000 A fabrication of NMR—microsensors for nanoliter sample volumes *Microelectron. Eng.* **53** 517–19
- [16] Olson D L, Lacey M E, Webb A G and Sweedler J V 1999 Nanoliter-volume H-1 NMR detection using periodic stopped-flow capillary electrophoresis *Anal. Chem.* **71** 3070–6
- [17] Bowtell R W, Brown G D, Glover P M, McJury M and Mansfield P 1990 Resolution of cellular structures by NMR microscopy at 11.7-T *Phil. Trans. R. Soc. London A-Math. Phys. Eng. Sci.* **333** 457–67
- [18] Glover P M, Bowtell R W, Brown G D and Mansfield P 1994 A microscope slide probe for high-resolution imaging at 11.7 T *Magn. Reson. Medicine* **31** 423–8
- [19] Wind R A *et al* 2000 An integrated confocal and magnetic resonance microscope for cellular research *J. Magn. Reson.* **147** 371–7
- [20] Roffmann W U, Gross D, Crozier S, Wilson S, Luescher K, Doddrell D M, Lehmann V and Zick K 1999 Hardware developments for *in-vivo* MR microscopy at fields up to 17.6 T *L14, In Book of Abstracts for 5th International Conf. on Magnetic Resonance Spectroscopy (Heidelberg)*

- [21] Xia Y 1998 Relaxation anisotropy in cartilage by NMR microscopy (μ MRI) at 14- μ m resolution *Magn. Reson. Medicine* **39** 941–9
- [22] Bowtell R and Robyr P 1998 Multilayer gradient coil design *J. Magn. Reson.* **131** 286–94
- [23] Seeber D A, Hoftiezer J H, Daniel W B, Rutgers M A and Pennington C H 2000 Triaxial magnetic field gradient system for microcoil magnetic resonance imaging *Rev. Sci. Instrum.* **71** 4263–72
- [24] Zhang W R and Cory D G 1998 Pulsed gradient NMR probes for solid state studies *J. Magn. Reson.* **132** 144–9
- [25] Simon B, Kimmich R and Kostler H 1996 Rotating-frame-imaging technique for spatially resolved diffusion and flow studies in the fringe field of RF probe coils *J. Magn. Reson. A* **118** 78–83
- [26] Valtier M, Humbert F and Canet D 1999 Maps of self-diffusion coefficients by radiofrequency field gradient NMR microscopy *J. Magn. Reson.* **141** 7–17
- [27] Köckenberger W 2001 Functional imaging of plants by magnetic resonance experiments *Trends Plant Sci.* **6** 286–92
- [28] Heidenreich M, Köckenberger W, Kimmich R, Chandrakumar N and Bowtell R W 1998 Investigation of carbohydrate metabolism and transport in castor bean seedlings by cyclic J cross polarization imaging and spectroscopy *J. Magn. Reson.* **132** 109–24
- [29] Olt S, Krotz E, Komor E, Rokitta M and Haase A 2000 Na-23 and H-1 NMR microimaging of intact plants *J. Magn. Reson.* **144** 297–304
- [30] Haishi T, Uematsu T, Matsuda Y and Kose K 2001 Development of a 1.0 T MR microscope using a Nd-Fe-B permanent magnet *Magn. Reson. Imaging* **19** 875–80
- [31] Peters A M and Bowtell R W 1999 Resolution in high field echo planar microscopy *J. Magn. Reson.* **137** 196–205
- [32] Lee S C, Kim K, Kim J, Lee S, Yi J H, Kim S W, Ha K S and Cheong C 2001 One micrometer resolution NMR microscopy *J. Magn. Reson.* **150** 207–13
- [33] Grant S C, Buckley D L, Gibb S, Webb A G and Blackband S J 2001 MR microscopy of multicomponent diffusion in single neurons *Magn. Reson. Medicine* **46** 1107–12
- [34] Hogers B, Gross D, Lehmann V, De Groot H J M, De Roos A, Gittenberger-De Groot A C and Poelmann R E 2001 Magnetic resonance microscopy at 17.6 T on chicken embryos *in vitro* *J. Magn. Reson. Imaging* **14** 83–6
- [35] Bauer W R, Hiller K H, Galuppo P, Neubauer S, Kopke J, Haase A, Waller C and Ertl G 2001 Fast high-resolution magnetic resonance imaging demonstrates fractality of myocardial perfusion in microscopic dimensions *Circulation Res.* **88** 340–6
- [36] Gardner J R, Hess C P, Webb A G, Tsika R W, Dawson M J and Gulani V 2001 Magnetic resonance microscopy of morphological alterations in mouse trabecular bone structure under conditions of simulated microgravity *Magn. Reson. Medicine* **45** 1122–5
- [37] Demco D E and Blümich B 2000 Solid-state NMR imaging methods: I. Strong field gradients *Concepts Magn. Reson.* **12** 188–206
- [38] Demco D E and Blümich B 2000 Solid-state NMR imaging methods: II. Line narrowing *Concepts Magn. Reson.* **12** 269–88
- [39] Chingas G C, Miller J B and Garroway A N 1986 NMR images of solids *J. Magn. Reson.* **66** 530–5
- [40] Miller J B, Cory D G and Garroway A N 1990 Line-narrowing approaches to solid-state NMR imaging - pulsed gradients and 2nd averaging *Phil. Trans. R. Soc. London A-Math. Phys. Eng. Sci.* **333** 413–26
- [41] Cory D G, Vanos J W M and Veeman W S 1988 NMR images of rotating solids *J. Magn. Reson.* **76** 543–7
- [42] Samoilenko A A, Artemov D Y and Sibeldina L A 1988 Formation of sensitive layer in experiments on NMR subsurface imaging of solids *JETP Lett.* **47** 417–19
- [43] McDonald P J and Newling B 1998 Stray field magnetic resonance imaging *Rep. Prog. Phys.* **61** 1441–93
- [44] Glover P M, Aptaker P S, Bowler J R, Ciampi E and McDonald P J 1999 A novel high-gradient permanent magnet for the profiling of planar films and coatings *J. Magn. Reson.* **139** 90–7
- [45] Keddie J L, Gorce J P, Mallegol J, Wallin M, Barry A M, Ciampi E, Motiejauskaite A, Glover P M, McDonald P J and Weissenborn P K 2001 MR profiling of film formation and crosslinking in waterborne alkyd emulsions and emulsion paints *Abstracts of Papers of the Am. Chem. Soc.* **222** 246-PMSE (part 2)
- [46] Laity P R, Glover P M, Godward J, McDonald P J and Hay J N 2000 Structural studies and diffusion measurements of water-swollen cellophane by NMR imaging *Cellulose* **7** 227–46
- [47] Emid S and Creyghton J H N 1985 High resolution NMR imaging in solids *Physica B, C* **128** 81–3
- [48] Balcom B J, MacGregor R P, Beyea S D, Green D P, Armstrong R L and Bremner T W 1996 Single-point ramped imaging with T-1 enhancement (SPRITE) *J. Magn. Reson. A* **123** 131–4
- [49] Mastikhin I V, Balcom B J, Prado P J and Kennedy C B 1999 SPRITE MRI with prepared magnetization and centric k-space sampling *J. Magn. Reson.* **136** 159–68
- [50] Fang Z J, Hoepfel D and Winter K 2001 Application of single point imaging (SPI) to solid state materials *Magn. Reson. Imaging* **19** 501–3

- [51] Midzor M M, Wigen P E, Pelekhov D, Chen W, Hammel P C and Roukes M L 2000 Imaging mechanisms of force detected FMR microscopy *J. Appl. Phys.* **87** 6493–5
- [52] Barbic M 2002 Magnetic resonance diffraction using the magnetic field from a ferromagnetic sphere *J. Appl. Phys.* **91**(12) 9987–94
- [53] Ramanathan C and Bencsik M 2001 Measuring spatially resolved gas transport and adsorption in coal using MRI *Magn. Reson. Imaging* **19** 555–9
- [54] Pines A 2001 ‘Shining light’ on NMR and MRI in porous materials *Magn. Reson. Imaging* **19** 307–9
- [55] Kuethe D O, Caprihan A, Fukushima E and Waggoner R A 1998 Imaging lungs using inert fluorinated gases *Magn. Reson. Medicine* **39** 85–8
- [56] Chen X J, Chawla M S, Hedlund L W, Moller H E, Macfall J R and Johnson G A 1998 MR microscopy of lung airways with hyperpolarized He-3 *Magn. Reson. Medicine* **39** 79–84
- [57] Johnson G A, Cofer G P, Hedlund L W, Maronpot R R and Suddarth S A 2001 Registered H-1 and He-3 magnetic resonance microscopy of the lung *Magn. Reson. Medicine* **45** 365–70
- [58] Obrist W D, Thompson H K Jr, King C H and Wang H S 1967 Determination of regional cerebral blood flow by inhalation of ^{133}Xe *Circulation Res.* **20** 124–35
- [59] Duhamel G, Choquet P, Grillon E, Lamalle L, Leviet J L, Ziegler A and Constantinesco A 2001 Xenon-129 MR imaging and spectroscopy of rat brain using arterial delivery of hyperpolarized xenon in a lipid emulsion *Magn. Reson. Medicine* **46** 208–12